

POLITECNICO

MILANO 1863

Spacecraft Attitude Dynamics and Control

Final Project

Giulio Pacifici, matr. 944852



Contents

1	Introduction	2
1.1	Configuration	2
1.2	Sensors	2
1.3	Actuators	3
2	The Model	4
2.1	Attitude Dynamics	4
2.2	Disturbing Torques	4
2.3	Sensors	6
2.4	Actuators	7
3	Attitude Determination	8
4	Mission Overview	8
5	Control System	9
5.1	Torque Allocation	9
5.2	Extended State Observer	10
5.3	Detumbling	10
5.4	Slew Maneuver	10
5.5	Earth Pointing	10
6	Simulation Framework	12
7	Simulation Results	13
7.1	Uncontrolled Dynamics	13
7.2	Detumbling	14
7.3	Slew Maneuver	15
7.4	Earth Pointing	17
7.5	Off-Nominal Conditions	19
8	Conclusions	20

1 Introduction

In this report, the design of the Attitude Determination and Control System of a $6U$ CubeSat is presented. The satellite carries a Nadir pointing payload, which is fixed to the CubeSat.

1.1 Configuration

The satellite's configuration is depicted in Figure 1, it consists of a $3U \times 2U \times 1U$ central body, one pair of $3U \times 1U$ of solar panels, and one pair of $3U \times 2U$ of solar panels. Where $1U$ is equivalent to 10 cm .

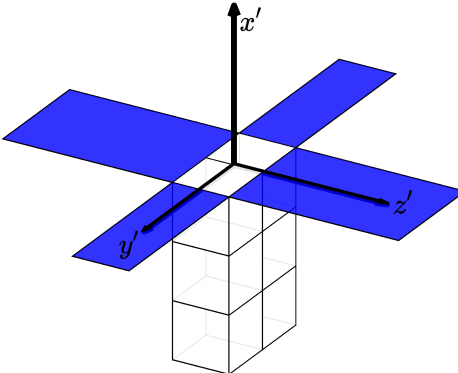


Figure 1: Representation of the $6U$ CubeSat.

The reference frame $\{x', y', z'\}$ is a geometrical frame in which the three axis are assumed to be parallel to the principal axis of inertia. The body frame $\{x, y, z\}$ is the principal inertia frame centered on the Center of Gravity (CG) of the satellite. The position of the CG is assumed to be shifted from the geometrical center of the body.

$$\mathbf{r}'_{CG} = \{-13, -2.5, -1\}^T \text{ cm}$$

The inertia matrix of the CubeSat is:

$$I = \begin{bmatrix} 6.2754346 \cdot 10^{-2} & 0 & 0 \\ 0 & 1.1345441 \cdot 10^{-1} & 0 \\ 0 & 0 & 1.617174 \cdot 10^{-1} \end{bmatrix} \text{ kg} \cdot \text{m}^2$$

The satellite is in a LEO orbit, the nominal keplerian elements are listed in Table 1.

Table 1: Nominal keplerian elements.

a	e	i	Ω	ω
6971 km	0.01	40°	0°	0°

Where a is the semi-major axis, e is the eccentricity, i is the inclination, Ω is the right ascension of the ascending node, and ω is the argument of perigee.

1.2 Sensors

The satellite is equipped with a star sensor, a magnetometer and a gyroscope.

The specifications of the **star sensor** are taken from the datasheet of the *T1 Star Tracker* produced by *TERMA* [8].

The cross-boresight accuracy is $\sigma_{cb} = 1.5''$, the roll-boresight accuracy is $\sigma_{rb} = 9''$.

**Table 2:** Star sensor specifications.

Max. Update Rate	F.O.V.	Max. Slew Rate	Size	Power
10 Hz	20°	0.5°/s	100 × 100 × 40 mm ³	2.5 W

The position of the star sensor (in the geometrical frame) is $\mathbf{r}'_{SS} = \{0, 0, 0\}^T$. The boresight direction of the sensor is coincident with the x axis of the body frame and with the z axis of the sensor's local frame. The rotation matrix from the sensor frame to the body frame is:

$$A_{b/s} = \begin{bmatrix} 0 & 0 & 1 \\ 1 & 0 & 0 \\ 0 & 1 & 0 \end{bmatrix}$$

The specifications of the **magnetometer** are taken from the datasheet of the *NMRM – Bn25o485* produced by *NewSpace Systems* [7].

Table 3: Magnetometer specifications.

Max. Update Rate	Noise	Orthogonality	Size	Power
18 Hz	16nT	< ±1°	99 × 43 × 17 mm ³	< 750 mW

The specifications of the **gyroscope** are taken from the datasheet of the *STIM300 IMU* produced by *Sensonor* [6].

Table 4: Gyroscope specifications.

Max. Update Rate	ARW	RRW	Volume	Power
262 Hz	0.15°/√hr	0.0003°/hr ^{3/2}	35 cm ³	< 2 W

1.3 Actuators

The satellite is equipped with three magnetic coils and one reaction wheel.

The selected set of **magnetic coils** is the *SatBus MTQ* designed by *NanoAvionics* [5].

Table 5: Magnetic coils specifications.

Dipole Strength (x and y axis)	Dipole Strength (z axis)	Power
0.30 Am ²	0.34 Am ²	0.4 W

The **reaction wheel** mounted on the satellite is the medium size *CubeWheel* designed by *CubeSpace* [3].

Table 6: Reaction wheel specifications.

Max. Torque	Momentum Storage (@ max rpm)	Size	Power
0.001 Nm	0.01 Nms	28 × 28 × 26.1 mm ³	0.24 W



2 The Model

2.1 Attitude Dynamics

The spacecraft is modeled as a rigid body, the dynamics is integrated using the Euler's Equations.

$$I \frac{d\boldsymbol{\omega}}{dt} = I\boldsymbol{\omega} \times \boldsymbol{\omega} + \mathbf{M}_c + \mathbf{M}_d \quad (1)$$

Where $\boldsymbol{\omega}$ is the angular velocity of the satellite, \mathbf{M}_c is the control torque, and \mathbf{M}_d is the disturbing torque, all expressed in the body reference frame.

The values of the angular velocity obtained from the numerical integration of (1) are used to compute the attitude of the satellite, the direction cosines matrix is employed to express the attitude of the body frame with respect to the inertial frame. The differential equation that rules the evolution of the direction cosines matrix is reported in (2).

$$\frac{dA_{b/n}}{dt} = -[\boldsymbol{\omega} \wedge] A_{b/n} \quad (2)$$

Where $A_{b/n}$ is the rotation matrix from the inertial to the body frame, and $[\cdot \wedge]$ is the cross product matrix operator. In order to preserve the orthogonality of $A_{b/n}$, at each time step the output of the numerical integration of (2) is updated using a single step orthonormalization algorithm (equation (3)).

$$A_{b/n}^{\text{new}} = \frac{3}{2} A_{b/n}^{\text{old}} - \frac{1}{2} A_{b/n}^{\text{old}} A_{b/n}^{\text{old}T} A_{b/n}^{\text{old}} \quad (3)$$

2.2 Disturbing Torques

The disturbing torques included in the model are the gravity gradient torque, the magnetic torque, the solar radiation pressure torque, and the drag torque. The models of the disturbing torques require the knowledge of the position vector and/or the velocity vector of the satellite along its orbit.

The orbit is integrated considering an unperturbed model. Thus the keplerian elements don't vary with time, except for the true anomaly which is governed by equation (4).

$$\dot{\theta} = \sqrt{\frac{\mu}{a^3}} \frac{(1 + e \cos \theta)^2}{(1 - e^2)^{3/2}} \quad (4)$$

Where μ is the gravitational parameter of the Earth ($398600 \text{ km}^3/\text{s}^2$). The position vector \mathbf{r}_{sc} and velocity vector \mathbf{v}_{sc} are computed in the inertial frame. The rotation matrix from the inertial to the Local Vertical Local Horizontal (*LVLH*) frame is computed as:

$$A_{l/n} = \begin{bmatrix} \cos \theta & \sin \theta & 0 \\ -\sin \theta & \cos \theta & 0 \\ 0 & 0 & 1 \end{bmatrix} \begin{bmatrix} 1 & 0 & 0 \\ 0 & \cos i & \sin i \\ 0 & -\sin i & \cos i \end{bmatrix}$$

The uncertainties on $A_{l/n}$, \mathbf{r}_{sc} , and \mathbf{v}_{sc} are neglected, thus it is assumed that these quantities are known exactly.

The torque due to **gravity gradient** is computed as:

$$\mathbf{M}_{GG} = \frac{3\mu}{||\mathbf{r}_{sc}||^3} \begin{Bmatrix} (I_z - I_y) c_2 c_3 \\ (I_x - I_z) c_1 c_3 \\ (I_y - I_x) c_2 c_1 \end{Bmatrix} \quad (5)$$

Where: $\begin{Bmatrix} c_1 \\ c_2 \\ c_3 \end{Bmatrix} = A_{b/n} A_{l/n}^T \begin{Bmatrix} 1 \\ 0 \\ 0 \end{Bmatrix} = A_{b/l} \begin{Bmatrix} 1 \\ 0 \\ 0 \end{Bmatrix}$.



In order to compute the **magnetic** torque, a dipole model of the Earth's magnetic field is implemented. This model represents a strong simplification of the actual magnetic field for the altitude involved, the model of the International Geomagnetic Reference Field (*IGRF*) [9] should be considered for more accurate simulations. The magnetic field vector in inertial frame is computed as:

$$\mathbf{B}_n = \frac{R_E^3 H_0}{||\mathbf{r}_{sc}||^3} [3(\hat{\mathbf{m}} \cdot \hat{\mathbf{r}})\hat{\mathbf{r}} - \hat{\mathbf{m}}]$$

Where R_E is the Earth's radius, $\hat{\mathbf{r}}$ is the versor in the direction of \mathbf{r}_{sc} , and $\hat{\mathbf{m}}$ is the direction of the magnetic field. The latter can be computed as:

$$\hat{\mathbf{m}} = \begin{Bmatrix} \sin(11.5^\circ) \cos(\omega_E t) \\ \sin(11.5^\circ) \sin(\omega_E t) \\ \cos(11.5^\circ) \end{Bmatrix}$$

Where ω_E is the Earth's angular velocity about its axis of rotation. The term H_0 is computed from the first order Gaussian coefficients of the *IGRF* [9], such that:

$$H_0 = \sqrt{(g_0^1)^2 + (g_1^1)^2 + (h_1^1)^2}$$

The disturbing torque is:

$$\mathbf{M}_{magn} = \mathbf{D}_r \times A_{b/n} \mathbf{B}_n = \mathbf{D}_r \times \mathbf{B}_b$$

Where \mathbf{D}_r is the residual dipole of the satellite that is assumed to be $\mathbf{D}_r = \{0.05, 0.05, 0.05\}^T A/m^2$.

In order to evaluate the torque due to **solar radiation pressure**, the satellite's external surface is divided into several planar surfaces. The force acting on each of these plates can be computed as:

$$\mathbf{F}_{i,SRP} = -\frac{F_e}{c} A_i (\hat{\mathbf{S}}_b \cdot \hat{\mathbf{n}}_{b,i}) \left\{ (1 - \rho_{s,i}) \hat{\mathbf{S}}_b + \left[2\rho_{s,i} (\hat{\mathbf{S}}_b \cdot \hat{\mathbf{n}}_{b,i}) + \frac{2}{3}\rho_{d,i} \right] \hat{\mathbf{n}}_{b,i} \right\}$$

Where c is the speed of the light, A_i is area of the plate, $\hat{\mathbf{S}}_b$ is the versor in the direction of the Sun, $\hat{\mathbf{n}}_{b,i}$ is the normal to the plate, $\rho_{s,i}$ and $\rho_{d,i}$ are respectively the coefficients of specular and diffuse reflection. It is assumed that $\rho_{s,i} = 0.8$ for the solar panels, $\rho_{s,i} = 0.5$ for the surface of the central body, and $\rho_{d,i} = 0.1$ for all the surfaces. F_e is the power per unit surface that is assumed to be the sum of the direct solar radiation, the radiation reflected by the Earth and the direct Earth's radiation [1]:

$$F_e = 1358 + 500 + 117 = 1975 W/m^2$$

The assumption that all the incoming direction is summed along the direction of the Sun and the fact that the Earth's shadow is not modeled will result in an overestimation of the disturbing torque.

The Sun position is modeled according to a simplified model, for which the Sun direction in the body frame is computed as:

$$\hat{\mathbf{S}}_b = A_{b/n} \hat{\mathbf{S}}_n = A_{b/n} \begin{Bmatrix} \cos(n_{sun}t) \\ \sin(n_{sun}t) \cos(23.45^\circ) \\ \sin(n_{sun}t) \sin(23.45^\circ) \end{Bmatrix} \text{ where } n_{sun} = 2\pi/1 \text{ year}$$

The disturbing torque is computed as

$$\mathbf{M}_{SRP} = \sum \mathbf{r}_i \times \mathbf{F}_{i,SRP}$$

where \mathbf{r}_i is position of the geometrical center of the plate. The summation is performed over the panels for which $\hat{\mathbf{S}}_b \cdot \hat{\mathbf{n}}_{b,i} > 0$.



The **drag** force acting on each surface is computed as:

$$\mathbf{F}_{i, drag} = -\frac{1}{2} c_d A_i \rho ||\mathbf{v}_{rel,b}|| \mathbf{v}_{rel,b} \left(\hat{\mathbf{n}}_{b,i} \cdot \frac{\mathbf{v}_{rel,b}}{||\mathbf{v}_{rel,b}||} \right)$$

c_d is drag coefficient of each panel that is assumed to be 2.2. ρ is the air density which is assumed to be constant and equal to the air density at the altitude of 600 km, which is $1.454 \cdot 10^{-13} \text{ kg/m}^3$ according to the *CIRA72* model [2]. $\mathbf{v}_{rel,b}$ is the relative velocity between the satellite and the rotating atmosphere: $\mathbf{v}_{rel,b} = A_{b/n} (\mathbf{v}_{sc} - \boldsymbol{\omega}_E \times \mathbf{r}_{sc})$, where $\boldsymbol{\omega}_E$ is Earth's rotational angular velocity vector.

The torque due to atmospheric drag is:

$$\mathbf{M}_{drag} = \sum \mathbf{r}_i \times \mathbf{F}_{i, drag}$$

The summation is performed over the panels for which $\frac{\mathbf{v}_{rel,b}}{||\mathbf{v}_{rel,b}||} \cdot \hat{\mathbf{n}}_{b,i} > 0$.

The total disturbing torque is computed as:

$$\mathbf{M}_d = \mathbf{M}_{GG} + \mathbf{M}_{magn} + \mathbf{M}_{SRP} + \mathbf{M}_{drag}$$

2.3 Sensors

The **star sensor** is modeled considering the identification of 4 stars at the same time. The model of a star map is not included in the simulation. The direction versor of each star is simulated by generating two random angles α_i and β_i (with $i = 1, \dots, 4$) that determine the position of the i -th star in the reference frame of the sensor. The two random angles are generated with a uniform distribution such that $\alpha_i \in [-\theta_{FOV}/2, \theta_{FOV}/2]$ and $\beta_i \in [-\pi/2, \pi/2]$, where θ_{FOV} is the field of view. The first angle represents the angle between the star direction and the boresight (z axis), while the second one is the angle on the $x - y$ plane between the projection of the direction vector and the x axis. The direction vector is then computed as:

$$\mathbf{v}_s^i = \begin{Bmatrix} \sin \beta_i \cdot \cos \alpha_i \\ \sin \beta_i \cdot \sin \alpha_i \\ \cos \beta_i \end{Bmatrix}$$

The error on the measure of the direction of each star is simulated by rotating \mathbf{v}_s^i with a rotation matrix $A_{123}(\phi, \theta, \psi)$, where ϕ , θ and ψ are Euler angles generated with independent normal distributions centered on zero. The first two angles have a standard deviation equal to σ_{cb} as they simulate the cross-boresight error, the third one has a standard deviation equal to σ_b as it represents the roll-boresight error. Since the three angles are small, the three rotations can be assumed to be independent from each other.

The attitude determination algorithm requires the knowledge of the measured direction in the body frame ($\bar{\mathbf{v}}_b^i$) and the exact position of the star in the inertial frame (\mathbf{v}_n^i), this two quantities are computed as follows:

$$\bar{\mathbf{v}}_b^i = A_{b/s} A_{123}(\phi, \theta, \psi) \mathbf{v}_s^i \quad \mathbf{v}_n^i = A_{b/n}^T A_{b/s} \mathbf{v}_s^i$$

The presence of the Sun is modeled such that while the star is inside the field of view, the measurements from the star sensor can't be used for the attitude determination algorithm. This condition is verified whenever

$$A_{b/s}^T \hat{\mathbf{S}}_b \cdot \{0, 0, 1\}^T \geq \cos \frac{\theta_{FOV}}{2}$$

The presence of other bodies such as the Earth or the Moon inside the field of view of the sensor is not modeled.



The measurement of the **magnetometer** is modeled considering two types of error: an additive error on each component of the magnetic field and the error due to the non-orthogonality of the axes of the magnetometer. The additive error is a vector ϵ in which each component is generated with a normal distribution centered on zero having a standard deviation equal to the noise level of the sensor. The non-orthogonality of the sensor is modeled by applying a rotation matrix $A_{123}(\phi, \theta, \psi)$ where ϕ , θ and ψ are Euler angles generated with independent normal distributions centered on zero and standard deviation of 1° .

The measure of the magnetic field is computed as follows:

$$\bar{\mathbf{B}}_b = A_{123}(\phi, \theta, \psi) (\mathbf{B}_b + \epsilon)$$

The measurement of the **gyroscope** is modeled including two types of error that affect the components of the measured ω :

- A white noise \mathbf{n} with zero mean and standard deviation equal to $ARW/\sqrt{\tau_s}$, where τ_s is the gyroscope's sampling time.
- A bias term \mathbf{b} the time derivative of which is a white noise with zero mean and standard deviation equal to $RRW/\sqrt{\tau_s}$.

The term b is integrated in time starting from the initial condition $\mathbf{b}(0) = \{0.3, 0.3, 0.3\}^T \text{°}/\text{h}$. The measured angular velocity is computed as:

$$\boldsymbol{\omega}_m = \boldsymbol{\omega} + \mathbf{n} + \mathbf{b}$$

The sampling times of the sensors are reported in Table 7.

Table 7: Sampling times of the sensors.

	Star Sensor	Magnetometer	Gyroscope
Sampling Time [s]	0.1	0.0556	0.01

2.4 Actuators

The **magnetic coils** are assumed to be oriented along the axes of the body frame. They generate a dipole vector \mathbf{D} in which each component satisfies the condition $|D_i| \leq D_{i,max}$, where $D_{i,max}$ is the maximum dipole that each coil can provide. The control torque that the magnetic torquers exert on the satellite is computed in the body frame as follows:

$$\mathbf{M}_{MT} = \mathbf{D} \times \mathbf{B}_b$$

The spinning axis $\hat{\mathbf{a}}_{RW}$ of the **reaction wheel** is considered to be oriented as the body z axis, thus $\hat{\mathbf{a}}_{RW} = \{0, 0, 1\}^T$. The control torque provided by the actuator is computed as follows:

$$\mathbf{M}_{RW} = -\boldsymbol{\omega} \times h_r \hat{\mathbf{a}}_{RW} - M_r \hat{\mathbf{a}}_{RW}$$

Where h_r is the value of the relative angular momentum of the reaction wheel with respect to the spacecraft and M_r is the relative torque acting on the wheel. The differential equation that rules the evolution of h_r is $\dot{h}_r = M_r$, it is integrated starting from the initial condition $h_r = 0$. It is assumed that the value of h_r is measured exactly by the internal sensor of the actuator. The relative angular momentum and the relative torque must satisfy the following conditions on their maximum absolute value:

$$|M_r| < M_{r,max} \quad |h_r| < h_{r,max} \quad (6)$$



Where $M_{r,max}$ and $h_{r,max}$ are respectively the maximum torque and the momentum storage reported in Table 6. The second condition must be avoided since the reaction wheel would no longer be capable of providing any torque in absence of a desaturation mechanism.

It may happen that the torque required by the control system exceeds the limits imposed by the actuators. Whenever the first condition in (6) is met, M_r is set equal to $M_{r,max} \cdot \text{sign}(M_r)$. Concerning the magnetic coils, whenever the required magnetic dipole on the i -th coil exceeds its limit, D_i is set equal to $D_{i,max} \cdot \text{sign}(D_i)$.

The total control torque is:

$$\mathbf{M}_c = \mathbf{M}_{MT} + \mathbf{M}_{RW}$$

3 Attitude Determination

The attitude determination algorithm is based on the analytical solution of the Wabha's problem. Given the set of exact positions of the tracked stars in the inertial frame $\{\mathbf{v}_n^i\}$ and the set of the corresponding measures in the body frame $\{\bar{\mathbf{v}}_b^i\}$, the square matrix B is defined:

$$B = \frac{1}{4} \sum_i \bar{\mathbf{v}}_b^i \mathbf{v}_n^{iT}$$

The matrix B is decomposed with the singular value decomposition algorithm obtaining the matrices U and V such that $B = U \Sigma^T V^T$, where Σ is a diagonal matrix that contains the square roots of the eigenvalues of $B^T B$. The estimation of the matrix $A_{b/n}$ is then obtained as:

$$\bar{A}_{b/n} = U M V^T, \text{ with } M = \text{diag}(1, 1, \det U \det V)$$

The measurements from the magnetometer are not employed in the attitude determination algorithm because of the large errors involved compared to the star sensor measurements.

This algorithm is employed whenever the Sun is out of the field of the star sensor, otherwise a different approach is implemented. When the Sun enters the field of view, the filtered angular speed $\bar{\omega}$ coming from the Extended State Observer (described in 5.2) is used to propagate the matrix $\bar{A}_{b/n}$ by integrating equation (2). The last available sample of $\bar{A}_{b/n}$ computed using the measurements of the star sensor is set as the initial condition.

Another condition in which the measurements from the star sensor are not employed for the determination of the attitude is when the angular velocity of the satellite exceeds the maximum slew rate of the star sensor reported in Table 2.

4 Mission Overview

The mission objective is to achieve a constant alignment between the x axis of the body frame ($\hat{\mathbf{x}}_b$) and the x axis of the *LVLH* frame ($\hat{\mathbf{x}}_l$). The main performance parameter is the pointing error, which is defined as the angle between the two axis.

$$\text{Pointing Error} = \arccos(\hat{\mathbf{x}}_b^T \hat{\mathbf{x}}_l) = \arccos \left([1 \ 0 \ 0] A_{b/n} A_{l/n}^T \begin{bmatrix} 1 \\ 0 \\ 0 \end{bmatrix} \right) = \arccos(A_{b/l} \mathbf{1}_1)$$

The mission is composed by three control modes:

- **Detumbling.** The satellite's angular velocity must be reduced almost to zero starting from the initial conditions after the orbit injection.
- **Slew Maneuver.** The satellite must be re-oriented in order to reach the desired alignment between the body frame and the *LVLH* frame. The angular velocity at the end of the maneuver must match the angular velocity of the *LVLH* frame.



- **Earth Pointing.** Right after the satellite re-orientation, the pointing error must be reduced and maintained below 1°.

5 Control System

5.1 Torque Allocation

The ideal control torque \mathbf{M}_c^{id} computed following the logic detailed in this section is distributed among the available actuators. Two different strategies are implemented. In both cases, the coupling term between the satellite angular velocity and the reaction wheel's angular momentum is subtracted from \mathbf{M}_c^{id} :

$$\bar{\mathbf{M}}_c' = \mathbf{M}_c^{id} - (-\bar{\omega} \times h_r \hat{\mathbf{a}}_{RW})$$

The first strategy allows to distribute the torque such that the resulting control action is exactly the desired one. Since the magnetic coils are not capable of generating torque in the direction of the magnetic field, the component of $\bar{\mathbf{M}}_c'$ along $\bar{\mathbf{B}}_b$ is supplied by the reaction wheel.

$$M_r = -\frac{\bar{\mathbf{M}}_c' \cdot \bar{\mathbf{b}}}{\bar{\mathbf{b}} \cdot \hat{\mathbf{a}}_{RW}} \quad (7)$$

Where $\bar{\mathbf{b}}$ is the versor in the direction of $\bar{\mathbf{B}}_b$.

The control torque provided by the magnetic coils is: $\bar{\mathbf{M}}_c'' = \bar{\mathbf{M}}_c' - (-M_r \hat{\mathbf{a}}_{RW})$. This torque is perpendicular to the measured magnetic field, thus the magnetic dipole is computed as follows:

$$\mathbf{D} = \frac{\bar{\mathbf{B}} \times \bar{\mathbf{M}}_c''}{\|\bar{\mathbf{B}}\|^2} \quad (8)$$

The second allocation logic produces a control torque that approximates \mathbf{M}_c^{id} . The component of $\bar{\mathbf{M}}_c'$ on the plane perpendicular to $\bar{\mathbf{B}}_b$ is provided by the magnetic coils. \mathbf{D} is computed using equation (8) where $\bar{\mathbf{M}}_c''$ is substituted with $\bar{\mathbf{M}}_c'$. The remaining control action that has still to be allocated is $\bar{\mathbf{M}}_c'' = \bar{\mathbf{M}}_c' - \mathbf{D} \times \bar{\mathbf{B}}_b$. The reaction wheel produces a torque equal to the component of $\bar{\mathbf{M}}_c''$ along $\hat{\mathbf{a}}_{RW}$:

$$M_r = -\bar{\mathbf{M}}_c'' \cdot \hat{\mathbf{a}}_{RW}$$

Note that the measured angular velocities and magnetic field vector are here employed since the exact quantities are not known.

For both strategies the resulting estimated control torque is:

$$\bar{\mathbf{M}}_c = -\bar{\omega} \times h_r \hat{\mathbf{a}}_{RW} - M_r \hat{\mathbf{a}}_{RW} + \mathbf{D} \times \bar{\mathbf{B}}_b$$

The first strategy theoretically allows to approximate almost exactly the required torque, nevertheless equation (7) has a singularity for $\bar{\mathbf{b}} \cdot \hat{\mathbf{a}}_{RW} = 0$. Whenever the satellite is close to the singularity condition, thus when $\hat{\mathbf{a}}_{RW}$ has a small component along $\bar{\mathbf{b}}$, the torque required from the reaction wheel could become large. Even if the reaction wheel is capable of providing the component of the required torque along $\bar{\mathbf{b}}$, it would create a large undesired torque on the plane perpendicular to $\bar{\mathbf{b}}$ that has to be compensated by the magnetic coils. In this condition, the components of the magnetic dipole may reach saturation, thus the resulting control torque would be very different from the desired one.

Since this undesired condition is likely to be verified when relatively high torques and angular velocities are involved, the first strategy is applied to the Earth Pointing maneuver only.

5.2 Extended State Observer

The Extended State Observer (*ESO*) described in [4] is implemented in order to filter the measured angular velocity and to estimate the unknown disturbances acting on the satellite. The system (9) describes the time evolution of the estimated angular velocity $\bar{\omega}$ and the estimated disturbance torque $\bar{\mathbf{M}}_d$.

$$\begin{cases} \dot{\bar{\omega}} &= I^{-1} (I\bar{\omega} \times \bar{\omega} + \bar{\mathbf{M}}_c + \bar{\mathbf{M}}_d) + L_\omega (\omega_m - \bar{\omega}) \\ \dot{\bar{\mathbf{M}}}_d &= L_d (\omega_m - \bar{\omega}) \end{cases} \quad (9)$$

Where $L_\omega = 0.05$ and $L_d = 5.8 \cdot 10^{-4}$. The initial conditions for the integration of (9) are $\bar{\omega}(0) = \omega_m(0)$ and $\bar{\mathbf{M}}_d(0) = \{0, 0, 0\}^T$.

The term $\bar{\mathbf{M}}_d$ can be used to increase the robustness and the disturbance rejection capabilities of the control system, thus it is included in the control laws.

5.3 Detumbling

The detumbling phase starts with a spin rate damping control law. This control logic involves only the magnetic coils, thus the allocation strategies discussed above are not implemented. The analytical expression of the ideal control dipole is: $\mathbf{D}^{id} = -k_b \dot{\mathbf{B}}_b$. It is approximated assuming that the variation of \mathbf{B}_b is only due to the rotation of the satellite, thus $\dot{\mathbf{B}}_b \approx -\omega \times \mathbf{B}_b$. The control dipole is computed as:

$$\mathbf{D} = k_b \bar{\omega} \times \bar{\mathbf{B}}_b, \text{ with } k_b = 10^7$$

This control logic is not capable of completely detumble the satellite, thus once a sufficiently low angular velocity is achieved the control law is changed.

The second control law is a proportional law:

$$\mathbf{M}_c^{id} = -k_{prop} \bar{\omega} - \bar{\mathbf{M}}_d, \text{ with } k_{prop} = 0.01$$

5.4 Slew Maneuver

The slew maneuver re-orients the spacecraft in order to track the desired attitude. The desired angular velocity and direct cosines matrix are defined as:

$$\omega_d = \{0, 0, \dot{\theta}\}^T \quad A_d = A_{l/n}$$

Where $\dot{\theta}$ is known from (4). The error angular speed and the error direction cosines matrix are defined as:

$$\omega_e = \bar{\omega} - A_e \omega_d \quad A_e = \bar{A}_{b/n} A_d^T$$

A non-linear control law is implemented, which is derived in [4] using a Lyapunov control function.

$$\mathbf{M}_c^{id} = -k_1 \omega_e - k_2 (A_e^T - A_e)^V + \bar{\omega} \times I\bar{\omega} - \bar{\mathbf{M}}_d$$

Where $k_1 = 0.1$, $k_2 = 0.0001$, and $(A_e^T - A_e)^V = \{A_{e23} - A_{e32}, A_{e31} - A_{e13}, A_{e12} - A_{e21}\}^T$.

5.5 Earth Pointing

The Euler angles α_x, α_y and α_z are introduced in order to characterize the linearized attitude dynamics of the satellite with respect to the *LVLH* frame, such that:

$$A_{b/l}^{\text{lin}} = \begin{bmatrix} 1 & \alpha_z & -\alpha_y \\ -\alpha_z & 1 & \alpha_x \\ \alpha_y & -\alpha_x & 1 \end{bmatrix}$$



The state space realization of the linearized attitude dynamics (including gravity gradient) is reported in (10). The attitude dynamics is linearized considering a circular orbit with mean motion $n = \sqrt{\mu/a^3}$, this approximation is justified by the low eccentricity of the orbit.

$$\dot{\mathbf{x}} = A\mathbf{x} + B\mathbf{u}, \text{ with } \mathbf{x} = \{\alpha_x, \alpha_y, \alpha_z, \dot{\alpha}_x, \dot{\alpha}_y, \dot{\alpha}_z\}^T \quad (10)$$

Where:

$$A = \begin{bmatrix} 0 & 0 & 0 & 1 & 0 & 0 \\ 0 & 0 & 0 & 0 & 1 & 0 \\ 0 & 0 & 0 & 0 & 0 & 1 \\ -K_x n^2 & 0 & 0 & 0 & -n(K_x - 1) & 0 \\ 0 & -4K_y n^2 & 0 & n(K_y - 1) & 0 & 0 \\ 0 & 0 & -3K_z n^2 & 0 & 0 & 0 \end{bmatrix} \quad B = \begin{bmatrix} 0 & 0 & 0 \\ 0 & 0 & 0 \\ 0 & 0 & 0 \\ 1/I_x & 0 & 0 \\ 0 & 1/I_y & 0 \\ 0 & 0 & 1/I_z \end{bmatrix}$$

$$\text{Where } K_x = \frac{I_z - I_y}{I_x} = 0.77, K_y = \frac{I_z - I_x}{I_y} = 0.87 \text{ and } K_z = \frac{I_y - I_x}{I_z} = 0.31.$$

The estimation of the matrix $A_{b/l}$ is: $\bar{A}_{b/l} = \bar{A}_{b/n} A_{l/n}^T$. The Euler angles can be estimated from the components of $\bar{A}_{b/l}$:

$$\alpha_x \approx \frac{1}{2}(\bar{A}_{b/l\ 23} - \bar{A}_{b/l\ 32}) \quad \alpha_y \approx \frac{1}{2}(\bar{A}_{b/l\ 31} - \bar{A}_{b/l\ 13}) \quad \alpha_z \approx \frac{1}{2}(\bar{A}_{b/l\ 12} - \bar{A}_{b/l\ 21}) \quad (11)$$

The time derivatives of the three Euler angles are estimated as follows:

$$\begin{Bmatrix} \dot{\alpha}_x \\ \dot{\alpha}_y \\ \dot{\alpha}_z \end{Bmatrix} \approx \bar{A}_{b/l}^T \bar{\omega} - \begin{Bmatrix} 0 \\ 0 \\ \dot{\theta} \end{Bmatrix} \quad (12)$$

A Linear Quadratic Regulator (*LQR*) is implemented in order to achieve the desired pointing accuracy. The cost function J is introduced:

$$J = \frac{1}{2} \int_0^\infty (\mathbf{z}^T W_{zz} \mathbf{z} + \mathbf{u}^T W_{uu} \mathbf{u}) dt$$

Where $\mathbf{z} = \mathbf{x}$ is the selected performance to be minimized. The weighting matrices are selected according to the a maximum value approach.

$$W_{uu} = \text{diag}(\{1/u_{i,max}^2\}), \text{ with } \mathbf{u}_{max} = \{1, 1, 10\}^T \cdot 10^{-5} \quad (13)$$

$$W_{zz} = \text{diag}(\{1/z_{i,max}^2\}), \text{ with } \mathbf{z}_{max} = \{100, 100, 100, 1, 1, 1\}^T \cdot 10^{-4} \quad (14)$$

The design of the *LQR* is performed using the MATLAB function `lqr` and the optimal gain matrix is obtained such that: $\mathbf{M}_c^{id} = -G\bar{\mathbf{x}} - \bar{\mathbf{M}}_d$. Where $\bar{\mathbf{x}}$ is the state vector estimated using (11) and (12).

6 Simulation Framework

A block diagram of the system is reported in Figure 2.

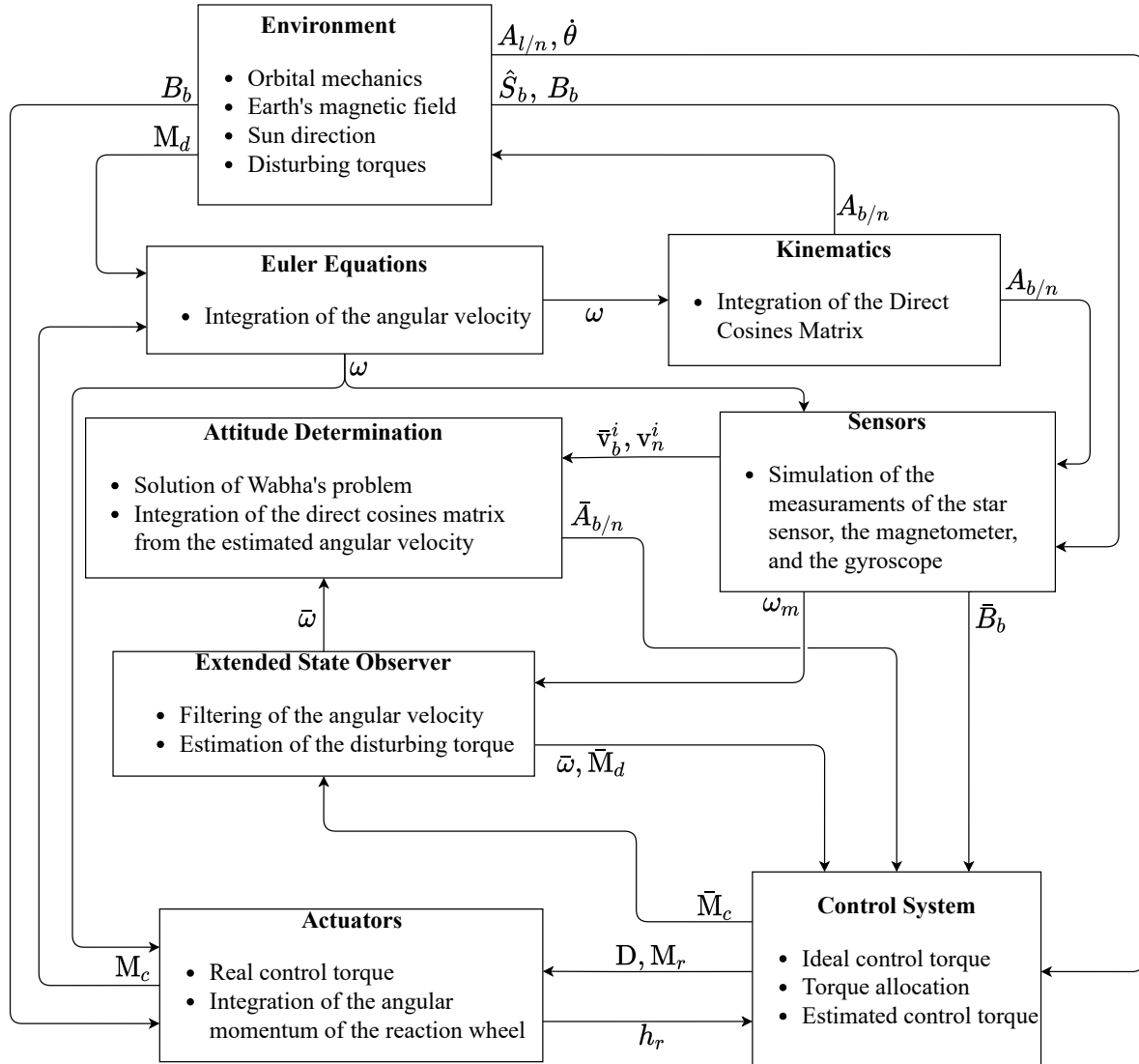


Figure 2: Simulation scheme.

The simulations are performed by integrating a numerical model implemented in Simulink which is based on this scheme. The integration algorithm used is the MATLAB's `ode15s`, the relative and absolute tolerances are set to 10^{-8} .

7 Simulation Results

The attitude dynamics of the satellite is first analyzed in the uncontrolled case, that is assuming that the actuators are not providing any control torque. The attitude dynamics is then simulated in nominal conditions for the three control modes described in 4. Finally, the robustness of the control system is evaluated in off-nominal conditions.

7.1 Uncontrolled Dynamics

The uncontrolled dynamics of the satellite is simulated for a time span of one orbital period starting from the following initial conditions.

$$\theta(0) = 0^\circ \quad A_{b/n}(0) = \mathbb{I}_3 \quad \omega(0) = \{10, -11, 8\}^T / s \quad (15)$$

The results are represented in Figure 3.

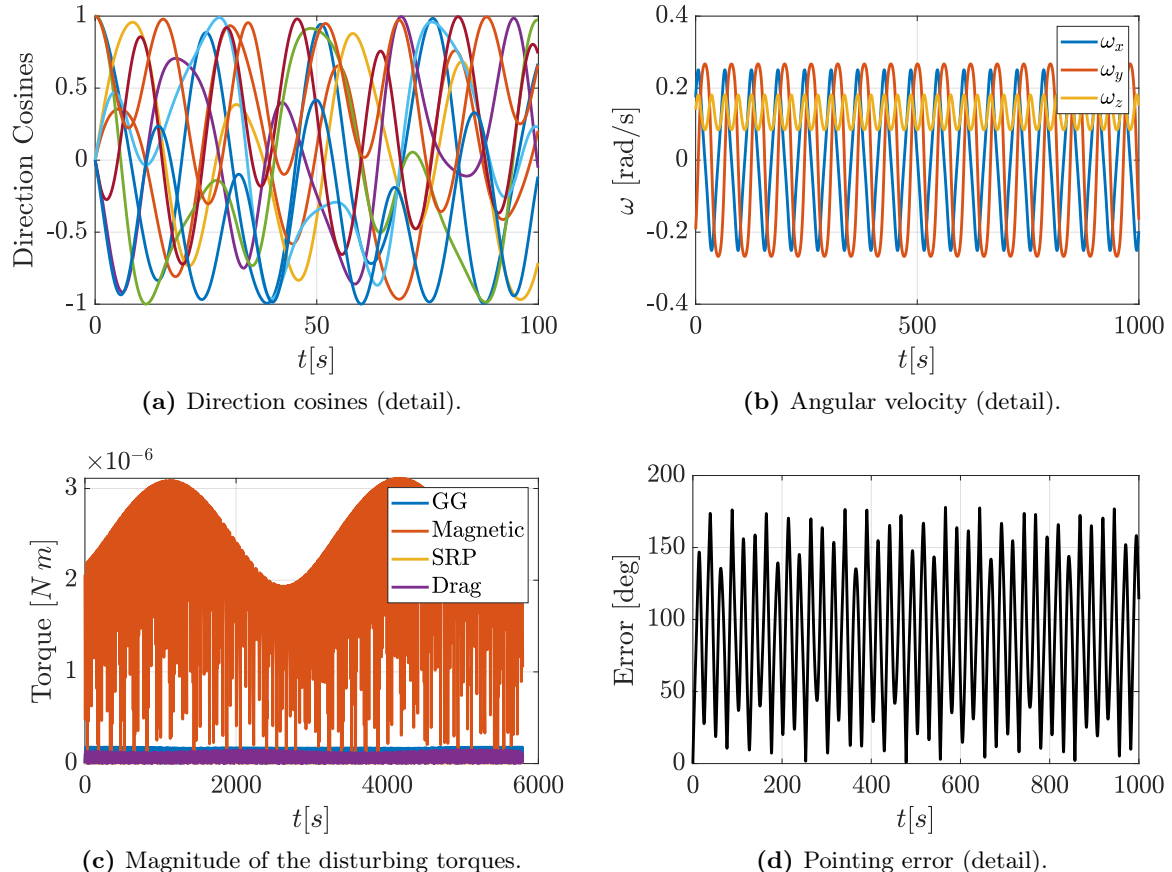


Figure 3: Dynamics of the uncontrolled satellite.

The four disturbing torques reach the maximum magnitudes reported in Table 8. The main

Table 8: Maximum magnitudes of the disturbing torques.

	M_{GG}	M_{magn}	M_{SRP}	M_{drag}
Max. Magnitude [Nm]	$1.8 \cdot 10^{-7}$	$3.1 \cdot 10^{-6}$	$6.9 \cdot 10^{-8}$	$1.5 \cdot 10^{-7}$

disturbing torque is the magnetic torque, due to the low altitude of the orbit. The torque due to the solar radiation pressure is negligible.

7.2 Detumbling

The detumbling phase starts at $t = 0\text{ s}$, the initial conditions are the same reported in (15). The spin rate damping lasts for 4000 s , while the proportional control lasts for 1000 s . The results reported in Figure 4 show that the control system is capable of reducing the angular velocity down to approximately $5 \cdot 10^{-3}\text{ }^\circ/\text{s}$.

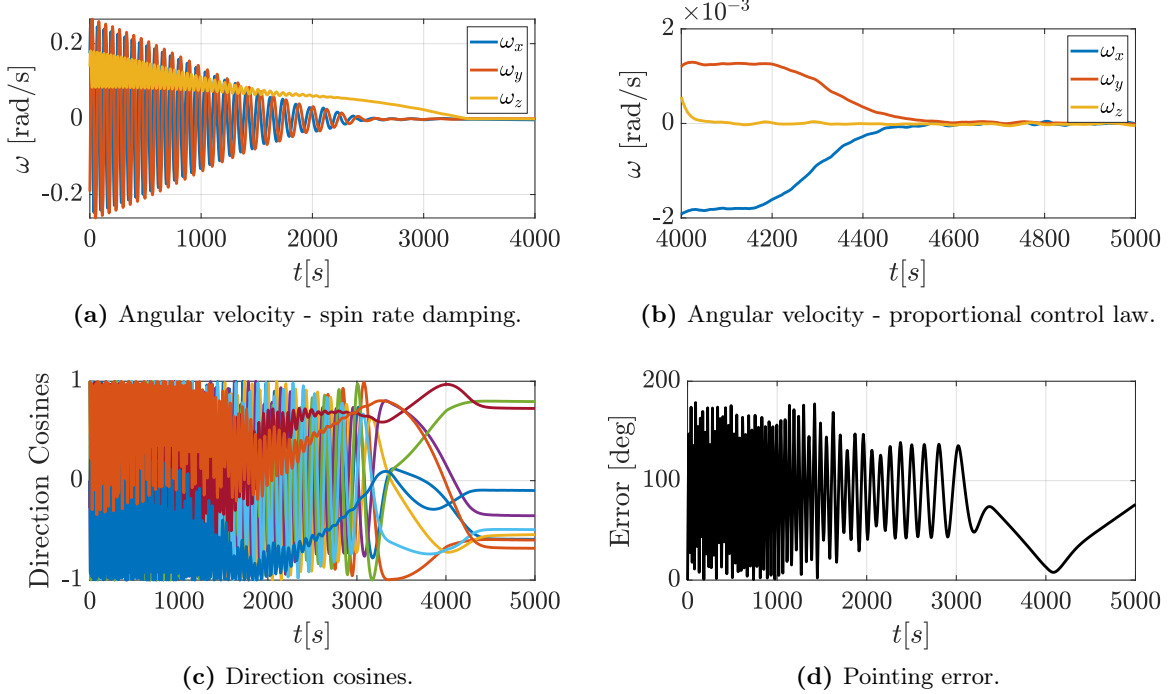


Figure 4: Satellite dynamics during detumbling phase.

The control torque acting on the satellite is represented in Figure 5 together with the difference between \mathbf{M}_c^{id} and \mathbf{M}_c during the proportional control phase. The z component of the ideal control torque is exactly provided thanks to the presence of the reaction wheel, while the differences are high for the x and y components. Since the magnetic coils are not saturated during the proportional control phase (Figure 6b), these differences are only due to the approximated torque allocation strategy. The errors due to the torque allocation are the cause of the slow response of x and y components of the angular velocity that can be observed in Figure 4b.

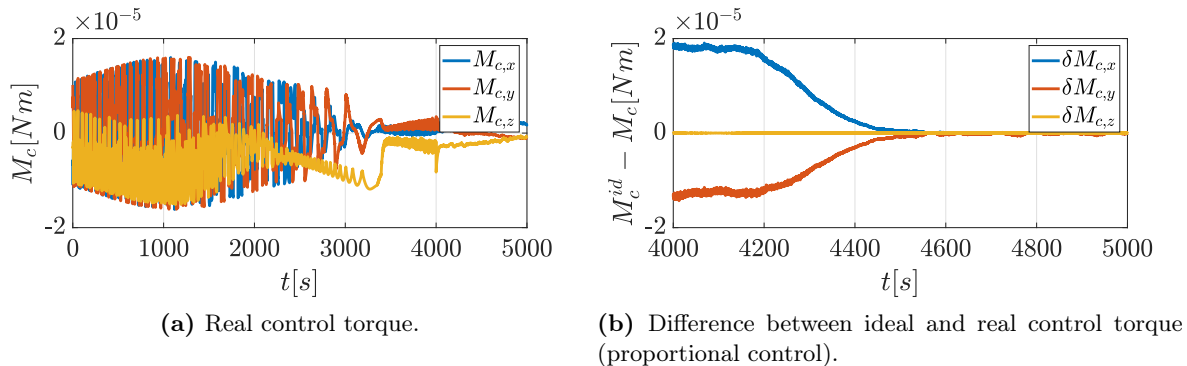
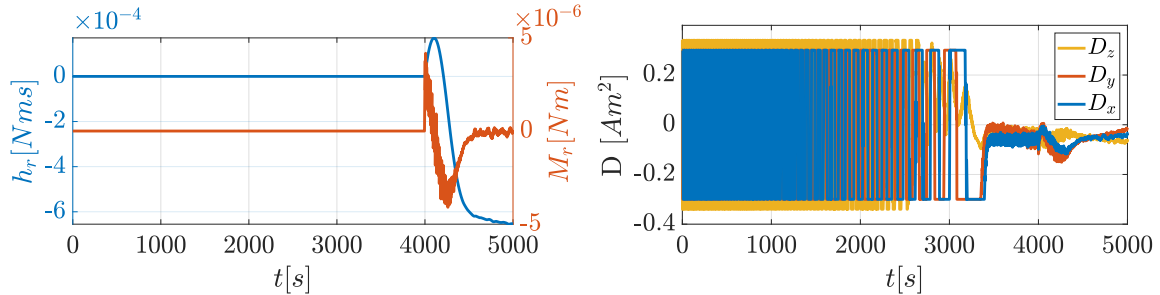


Figure 5: Control torque during detumbling.



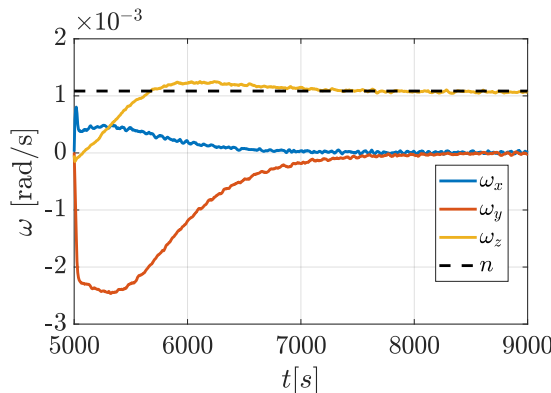
(a) Torque and angular momentum of the reaction wheel.

(b) Magnetic dipole of the magnetic coils.

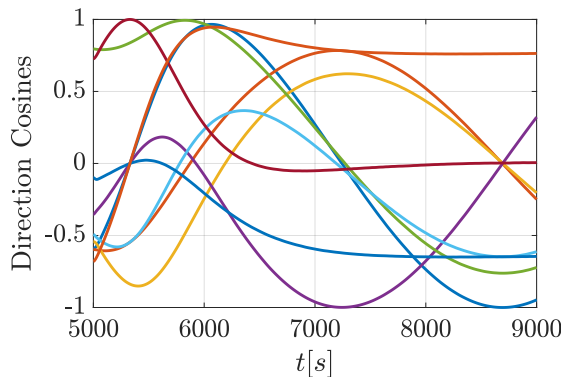
Figure 6: Dynamics of the actuators during detumbling.

7.3 Slew Maneuver

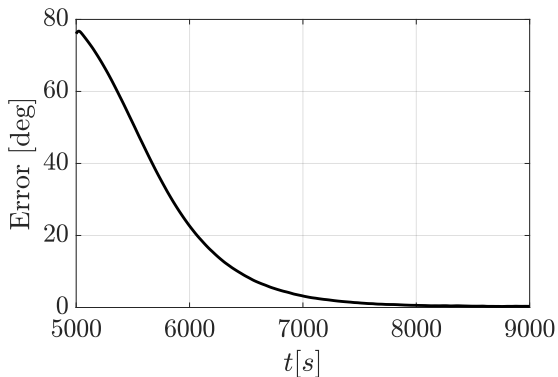
The slew maneuver starts at $t = 5000\text{ s}$, once the detumbling phase has ended. The results represented in Figure 7 show that the satellite is re-oriented in 4000 s , the angular velocity involved are relatively small. The third component of ω converges approximately to the the value of the mean orbital motion.



(a) Angular velocity.



(b) Direction cosines.



(c) Pointing error.

Figure 7: Satellite dynamics during slew maneuver.

The control torque (Figure 8a) is lower with respect to detumbling phase, the error with respect to the ideal control torque on the x and y axis is still high, especially in the first time instants.

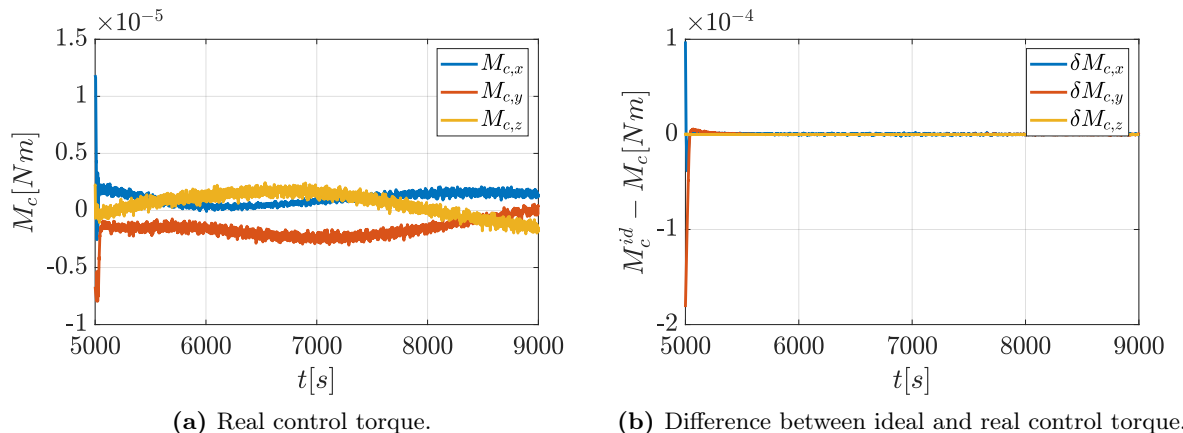


Figure 8: Control torque during slew maneuver.

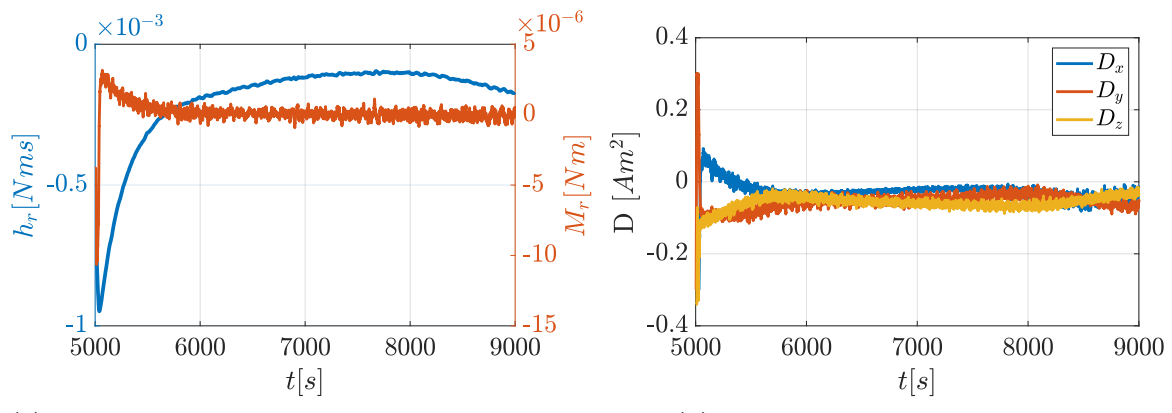


Figure 9: Dynamics of the actuators during slew maneuver.

7.4 Earth Pointing

The Earth pointing phase is simulated starting from the conditions after the slew maneuver for a time span of two orbital periods. The results in Figure 10 show that the control system satisfies the requirements on the pointing error.

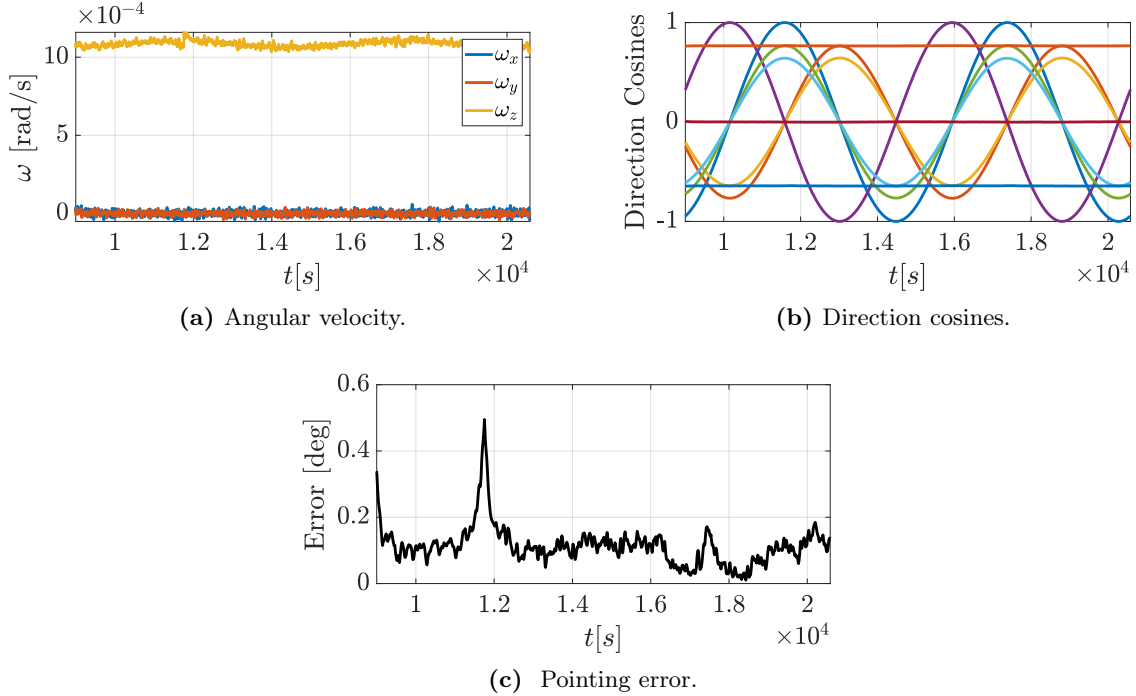


Figure 10: Satellite dynamics during Earth pointing.

The ideal control torque is well approximated (Figure 11b), thanks to the different torque allocation strategy applied during the Earth pointing phase. The control torque along z has higher peaks with respect to the other components (Figure 11a). This is explained by the higher value of the third component of \mathbf{u}_{max} reported in equation (13), that allows to exploit the larger control budget provided by the reaction wheel.

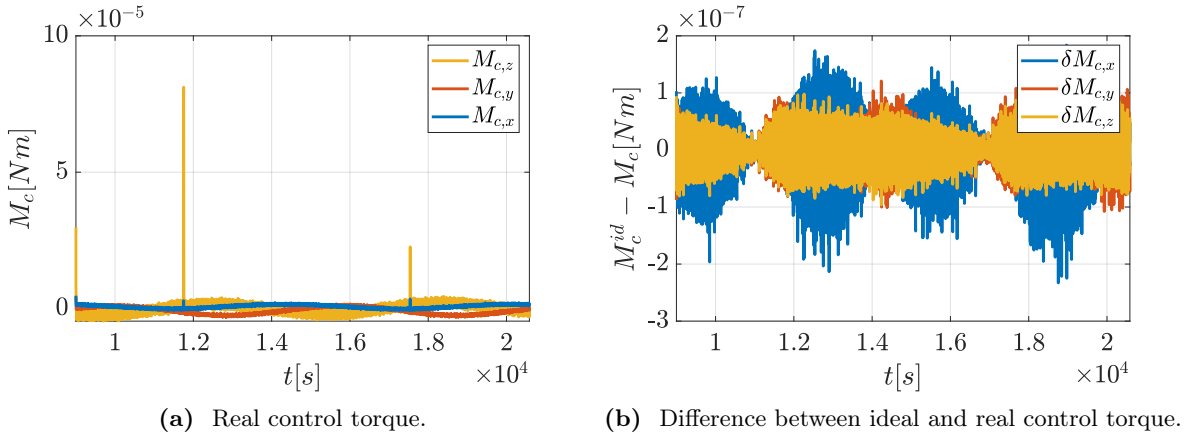
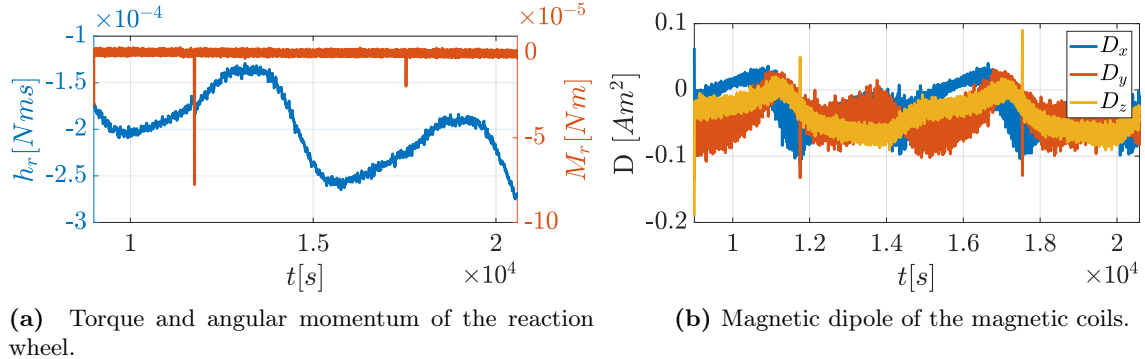


Figure 11: Control torque during Earth pointing.

The angular momentum of the reaction wheel in Figure 12a shows a constant increase, which is due to the fact that the actuator has to counteract the secular components of the disturbing torques. The secular evolution of the angular momentum implies that the reaction

wheel will eventually reach saturation, thus a desaturation mechanism is required in order to extend the duration of the mission.

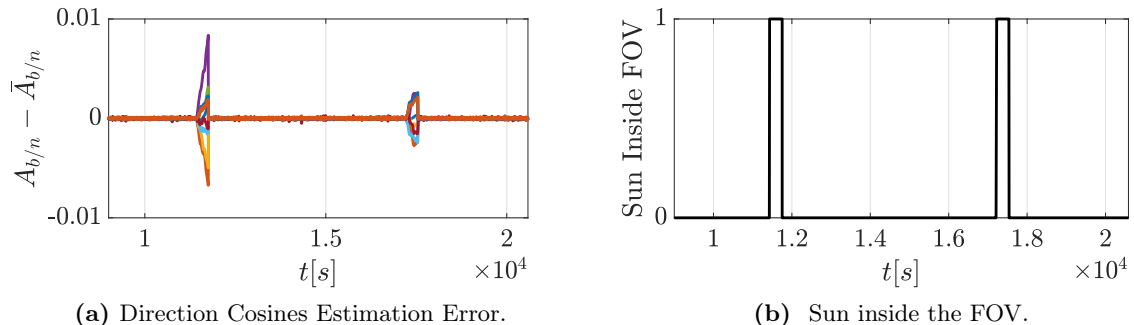


(a) Torque and angular momentum of the reaction wheel.

(b) Magnetic dipole of the magnetic coils.

Figure 12: Dynamics of the actuators during Earth pointing.

The performance of the attitude determination algorithm is represented in Figure 13a. It shows that the direction cosines are well estimated while the measurements of the star sensor are available, higher errors are instead present while the estimated angular velocity is integrated. Notice that the peaks in the pointing error and in the control torque are in correspondence of the time intervals during which the Sun is inside the field of view of the star sensor (Figure 13b).



(a) Direction Cosines Estimation Error.

(b) Sun inside the FOV.

Figure 13: Estimation of the Direction Cosines.

As for the performance of the Extended State Observer, the maximum estimation errors are reported in the first two columns of Table 9. The errors are approximately the 10% of the magnitude of the quantities to be estimated. A good filtering of the measurements of the gyroscope is achieved.

Table 9: Performance of the Extended State Observer.

$\max_t \mathbf{M}_d - \bar{\mathbf{M}}_d $	$\max_t \boldsymbol{\omega} - \bar{\boldsymbol{\omega}} $	$\max_t \boldsymbol{\omega} - \boldsymbol{\omega}_m $
$4 \cdot 10^{-7} Nm$	$7 \cdot 10^{-5} rad/s$	$2 \cdot 10^{-3} rad/s$

7.5 Off-Nominal Conditions

In order to assess the robustness of the control system, three additional cases are simulated. In each of these some parameters are changed with respect to the nominal case (Table 10).

Table 10: Conditions for the three cases.

	Case 1	Case 2	Case 3
$\omega(0) [^\circ/s]$	$\{7, -10, -8\}^T$	$\{3, 13, -9\}^T$	$\{-8, 9, -11\}^T$
$A_{b/n}(0)$	$\begin{bmatrix} 0.66 & 0.66 & -0.34 \\ 0.051 & 0.42 & 0.91 \\ 0.75 & -0.62 & 0.24 \end{bmatrix}$	$\begin{bmatrix} -0.7 & 0.7 & -0.1 \\ -0.67 & -0.61 & 0.42 \\ 0.23 & 0.37 & 0.9 \end{bmatrix}$	$\begin{bmatrix} -0.74 & 0.5 & -0.45 \\ -0.62 & -0.77 & 0.15 \\ -0.27 & 0.39 & 0.88 \end{bmatrix}$
$\mathbf{r}'_{cg} [cm]$	$\{-16, -2, 4\}^T$	$\{-13.5, 2, -4\}^T$	$\{-13.7, -3, 1\}^T$
c_d	2.5	2.5	2
$\mathbf{D}_r [Am^2]$	$\{0.1, 0.1, -0.1\}^T$	$\{0.1, 0.1, 0.1\}^T$	$\{0.1, 0.05, 0.1\}^T$
$I [kg \cdot dm^2]$	$\begin{bmatrix} 6.9 & -0.52 & -1.1 \\ -0.52 & 10.0 & -0.79 \\ -1.1 & -0.79 & 17.0 \end{bmatrix}$	$\begin{bmatrix} 6.1 & -0.36 & -2.3 \\ -0.36 & 11.0 & -0.5 \\ -2.3 & -0.5 & 19.0 \end{bmatrix}$	$\begin{bmatrix} 5.7 & 0.12 & 0.69 \\ 0.12 & 10.0 & -0.82 \\ 0.69 & -0.82 & 19.0 \end{bmatrix}$

The three cases are simulated starting from $t = 0 s$, the time duration of the detumbling, slew maneuver and Earth pointing phases are the same for all the three cases in order to compare their responses. The results represented in Figure 14 show that the system satisfies the requirements also in off-nominal conditions.

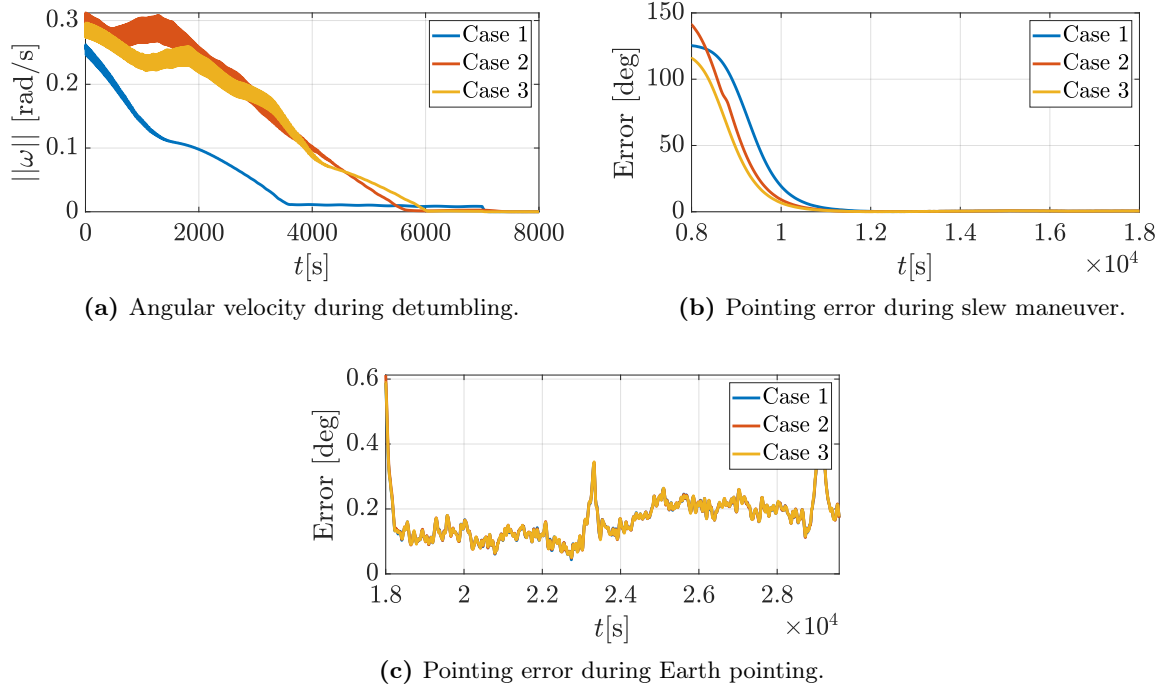


Figure 14: Comparison between the three cases.



The fact that the control system is based on the nominal inertia matrix introduces an additional source of disturbance. The effects of the uncertainties on the inertia matrix are included in the disturbing torque estimated by the Extended State Observer as described in [4].

It is also important to point out that the expression of \mathbf{M}_{GG} reported in equation (5) is valid only for a principal frame of inertia [1]. In this analysis the presence of extra-diagonal terms in I is neglected for the computation of \mathbf{M}_{GG} , thus (5) is still applied.

8 Conclusions

The simulations performed show that the control system satisfies the mission requirements reported in 4 both in nominal and off-nominal conditions. In particular, the pointing error during the Earth pointing phase is kept below the imposed limit with a large margin, conferring additional robustness to the system against unmodeled uncertainties.

The main critical issue of the control system is the presence of large errors in the approximation of the ideal control torque during the detumbling and slew maneuvers, which leads to a slow system response. This problem can be addressed by using more powerful actuators or by adding one or more reaction wheels. With three additional reaction wheels, the control system would be capable of providing the full required torque also in the event of the failure of one wheel.

Another major issue is attitude estimation when the measurements of star sensor can't be used. One possible solution is the introduction of an Earth horizon sensor that could be used in conjunction with a linear observer to estimate the attitude with respect to the *LVLH* frame.

The model of the system implemented for this project included all the main dynamics and disturbances of the real system, nevertheless the model can be refined in order to achieve more realistic simulations. Two improvements that could be introduced are the model of the *IGRF* (with a degree of accuracy greater than 1), and the model of the main perturbations of the orbital dynamics (i.e. *J2* effect and atmospheric drag).

References

- [1] F. Bernelli. *Lecture notes for the course "Spacecraft Attitude Dynamics and Control"*.
- [2] C. C. for the COSPAR International Reference Atmosphere. *CIRA 1972: COSPAR International Reference Atmosphere 1972*. Akademie-Verlag, 1972.
- [3] CubeSpace. *CubeWheel Reaction/Momentum Wheel*. URL: <https://www.cubespace.co.za/products/adcs-components/cubewheel/> (visited on 12/30/2020).
- [4] B. J. Douglas. *Lecture notes for the course "Spacecraft Attitude Dynamics and Control"*.
- [5] NanoAvionics. *CubeSat Magnetorquer SatBus MTQ*. URL: <https://nanoavionics.com/cubesat-components/cubesat-magnetorquer-satbus-mtq/> (visited on 12/30/2020).
- [6] Senonor. *STIM300 - Sensor Datasheet*. URL: <https://www.senor.com/products/inertial-measurement-units/stim300/> (visited on 12/30/2020).
- [7] N. Systems. *NMRRM-Bn250485 - Sensor Datasheet*. URL: <https://www.newspacesystems.com/portfolio/magnetometer/> (visited on 12/30/2020).
- [8] TERMA. *T1 & T2 Star Trackers - Miniaturized Optical Heads and Electronic Unit*. URL: https://www.terma.com/media/437079/t1_t2_star_tracker_rev2.pdf (visited on 12/30/2020).
- [9] E. Thebault et al. "International Geomagnetic Reference Field: the 12th generation". In: (2015).